

Phase-function normalization for accurate analysis of ultrafast collimated radiative transfer

Brian Hunter and Zhixiong Guo*

Department of Mechanical and Aerospace Engineering, Rutgers, the State University of New Jersey,
98 Brett Road, Piscataway, NJ 08854, USA

*Corresponding author: guo@jove.rutgers.edu

Received 12 October 2011; revised 10 February 2012; accepted 20 February 2012;
posted 22 February 2012 (Doc. ID 156418); published 20 April 2012

The scattering of radiation from collimated irradiation is accurately treated via normalization of phase function. This approach is applicable to any numerical method with directional discretization. In this study it is applied to the transient discrete-ordinates method for ultrafast collimated radiative transfer analysis in turbid media. A technique recently developed by the authors, which conserves a phase-function asymmetry factor as well as scattered energy for the Henyey–Greenstein phase function in steady-state diffuse radiative transfer analysis, is applied to the general Legendre scattering phase function in ultrafast collimated radiative transfer. Heat flux profiles in a model tissue cylinder are generated for various phase functions and compared to those generated when normalization of the collimated phase function is neglected. Energy deposition in the medium is also investigated. Lack of conservation of scattered energy and the asymmetry factor for the collimated scattering phase function causes overpredictions in both heat flux and energy deposition for highly anisotropic scattering media. In addition, a discussion is presented to clarify the time-dependent formulation of divergence of radiative heat flux. © 2012 Optical Society of America

OCIS codes: 000.4430, 030.5620, 170.3660, 290.7050.

1. Introduction

Many laser applications involve the transport of radiative energy through turbid media, including the interaction of light with biological tissue during laser microsurgery, diffuse optical tomography, or other biomedical laser therapeutic applications [1–7]. It is imperative that accurate solutions of the equation of radiative transfer (ERT) are determined. As an integro-differential equation, the ERT is almost impossible to solve analytically except when cases are extremely simplified. As such, numerical methods are commonly adopted so that radiation intensities, heat fluxes, and other radiative properties can be determined. There have been many proposed methods to solve the ERT, including the finite volume method (FVM) [8], radiation element method [9], and YIX

method [10]. However, one of the more well-known and commonly used methods, due to its relative simplicity for numerical implementation, is the discrete ordinates method (DOM), introduced in 1968 by Carlson and Lathrop [11].

Since the advent of ultrafast lasers, the study of ultrafast radiative heat transfer in turbid media has attracted increasing attention [3–7, 12–15]. The ultrafast radiative transfer is defined as that the ERT is time-dependent and radiation propagates with the speed of light in an ultrashort time scale [9]. It is different from the conventional transient radiative transfer in that only the boundary condition is time-dependent, but the ERT is still stationary. The introduction of a time-dependent term in the ERT transforms the equation into a hyperbolic format, complicating the modeling of the already sophisticated integro-differential ERT. Kumar, Mitra, and Guo were pioneers in this field, examining the transport of short light pulses through one-dimensional

planar scattering—absorbing media using different approximate mathematical models [3] or using the TDOM to solve the time-dependent ERT in two- and three-dimensional geometries [12,13]. Guo and coauthors further extended the study to applications including laser-tissue welding and soldering and hyperthermia therapy [4,7], three-dimensional optical imaging [5], laser ablation of cancerous cells [14], and treatment of pulse train irradiation using Duhamel’s superposition theorem [13,15].

In turbid media, such as biological tissue, the scattering of light can be highly anisotropic. Caution must be taken to ensure that scattered energy remains conserved after directional discretization. To ensure the conservation of anisotropically scattered energy, phase function normalization is generally adopted. Previously published techniques by Kim and Lee [16] and Wiscombe [17] have been crafted to exactly conserve scattered energy after DOM discretization, no matter the quadrature scheme adopted. However, a more recent publication by Boulet *et al.* [18] determined that even though scattered energy was in fact conserved using these techniques, the overall phase-function asymmetry factor and phase-function shape were distorted greatly for strongly forward-scattering functions, resulting in substantial skewing of heat flux profiles as compared to those generated with the Monte Carlo method.

To this end, Hunter and Guo [19,20] developed a new phase-function normalization technique, which was crafted to specifically conserve both the phase-function asymmetry factor and scattered energy simultaneously. They applied this technique both to the DOM [19] and the FVM [20]. The previous works by Hunter and Guo, however, only considered diffuse irradiation. When collimated irradiation in scattering media is concerned, the radiation consists of two components—collimated (ballistic) and diffuse, leading to the necessity of investigating the impact of implementing phase-function normalization on the collimated scattering phase function in addition to the normalization of the diffuse counterpart. Moreover, the previous studies focused on normalization of Henyey–Greenstein phase function. There is a need to examine the technique for general Legendre scattering phase functions.

In this study, the TDOM with phase-function normalization is implemented to predict ultrafast radiative transfer in a biological tissue sample subject to collimated laser incidence. Conservation of both scattered energy and the asymmetry factor are examined for the diffuse and collimated scattering phase functions after directional discretization. Results generated for a basic cylindrical enclosure are compared to previously published results for validation. Steady-state and transient heat flux profiles, generated both with and without collimated phase-function normalization, are compared for various phase functions to determine the impact of collimated phase-function normalization. The impact of location and asymmetry factor on energy deposition in the medium is also

investigated. In addition, a new formulation of divergence of radiative heat flux for ultrafast radiation transfer, communicated by Rath and Mahapatra [21], is discussed and clarified.

2. Radiative Transfer Equation

In general vector notation, the time-dependent ERT for a diffuse, gray, absorbing-emitting and scattering enclosure can be written as follows [22]:

$$\frac{1}{c} \frac{\delta I(\mathbf{r}, \hat{\mathbf{s}}, t)}{\delta t} + \hat{\mathbf{s}} \cdot \nabla I(\mathbf{r}, \hat{\mathbf{s}}, t) = -\beta I(\mathbf{r}, \hat{\mathbf{s}}, t) + \sigma_a I_b(\mathbf{r}, t) + \frac{\sigma_s}{4\pi} \int_{4\pi} I(\mathbf{r}, \hat{\mathbf{s}}', t) \Phi(\hat{\mathbf{s}}', \hat{\mathbf{s}}) d\Omega', \quad (1)$$

where c is the speed of light in the medium, $I(\mathbf{r}, \hat{\mathbf{s}}, t)$ is the radiative intensity propagating in radiation direction $\hat{\mathbf{s}}$ at location \mathbf{r} at time t , $I_b(\mathbf{r}, t)$ represents the blackbody intensity of the medium, $\Phi(\hat{\mathbf{s}}', \hat{\mathbf{s}})$ is the scattering phase function from direction $\hat{\mathbf{s}}'$ to direction $\hat{\mathbf{s}}$, and the extinction coefficient β is the sum of the medium absorption coefficient σ_a and scattering coefficient σ_s . The two terms on the left-hand side of the ERT represent the temporal and spatial gradients of radiative intensity. The first term on the right-hand side accounts for intensity attenuation due to absorption and scattering, the second term for blackbody emission, and the third term for radiant energy gain due to in-scattering.

Consider an axisymmetric cylindrical sample of biological tissue, with radius R and depth H , subject to a normal collimated incidence of magnitude I^C (excluding reflectance) at the top surface ($z = 0^+$). Using the TDOM, Eq. (1) can be expressed, for a discrete direction l , as follows [4,23]:

$$\frac{1}{c} \frac{\delta I^l}{\delta t} + \frac{\mu^l}{r} \frac{\delta}{\delta r} [rI^l] - \frac{1}{r} \frac{\delta}{\delta \phi} [\eta^l I^l] + \xi^l \frac{\delta I^l}{\delta z} = -\beta I^l + \beta S^l. \quad (2)$$

The direction cosines μ^l , η^l , and ξ^l correspond to the r , ϕ , and z directions, respectively. When collimated irradiation is considered, the source term S^l can be expanded into three components, as follows:

$$S^l = (1-\omega)I_b + \frac{\omega}{4\pi} \sum_{l'=1}^M w^{l'} \Phi^{l'l} I^{l'} + \frac{\omega}{4\pi} I^C \Phi^{l^C l} \exp(-\tau_z), \quad (3)$$

where the second term is the angular directional discretization of the integral term in Eq. (1). In said terms, $\omega = \sigma_s/\beta$ is the single scattering albedo, M is the total number of discrete directions analyzed using the DOM, $w^{l'}$ is the DOM quadrature weight corresponding to direction l' , and $\Phi^{l'l}$ is the diffuse scattering phase function between directions l' and l . The third term represents the propagation and scattering of the collimated incidence, where $\Phi^{l^C l}$ is the collimated scattering phase function from the direction of collimated incidence l^C to direction l , and the optical depth $\tau_z = \beta z$ ranges from $\tau_0 = 0$

at the top incident surface to $\tau_H = \beta H$ at the bottom cylinder surface.

There are three types of boundary conditions to be considered for the biological tissue cylinder. At the radial centerline, an axisymmetric condition (perfect mirror) is imposed. At the collimated incident surface ($z = 0$), a Fresnel reflection boundary condition is imposed due to the mismatch between the refractive indices of the tissue and surrounding air. The surface at $z = 0$ is taken to be a specular reflector, with the intensity emanating from any point w on the surface in direction l calculated as follows [4,12]:

$$I_w^l = (1 - \rho_{w,s}^l) I_{bw} + \rho_{w,s}^l I^{-l}, \quad (4)$$

where the incoming direction $-l$ has direction cosines $\mu^{-l} = \mu^l$ and $\xi^{-l} = -\xi^l$. The specular reflectivity $\rho_{w,s}^l$ is evaluated as

$$\rho_{w,s}^l = \begin{cases} \frac{1}{2} \left[\frac{\tan^2(\theta_i^l - \theta_r^l)}{\tan^2(\theta_i^l + \theta_r^l)} + \frac{\sin^2(\theta_i^l - \theta_r^l)}{\sin^2(\theta_i^l + \theta_r^l)} \right], & \theta_i^l < \theta_{cr}, \\ 1, & \theta_i^l \geq \theta_{cr}, \end{cases} \quad (5)$$

where θ_i^l is the angle of incidence of the incoming radiation, θ_r^l is the angle of refraction of the incoming radiation (determined via Snell's law), and $\theta_{cr} = \sin^{-1}(n_{\text{air}}/n_{\text{tissue}})$ is the critical angle determined from the refractive indices of air and tissue.

The boundaries at both the bottom axial and radial side walls ($z = H$ and $r = R$) are taken as diffuse reflectors. The intensity emanating from the bottom wall ($z = H$) can be calculated as a sum of blackbody emission, reflection of the collimated incidence, and diffuse reflection of all incoming intensities:

$$I_w^l = (1 - \rho_{w,d}) I_{bw} + \frac{\rho_{w,d}}{\pi} \left[I^C \exp(-\tau_H) + \sum_{l', \xi^{l'} < 0} w^{l'} I^{l'} |\xi^{l'}| \right], \quad \xi^l > 0, \quad (6)$$

where the diffuse reflectivity $\rho_{w,d}$ is taken to be 0.5 due to the highly scattering optical thickness of turbid tissue and the theory of random walk [12,13]. The boundary condition for the radial wall can be written in a similar manner, as long as the direction cosines are properly manipulated in the final term. For the radial wall, however, the collimated term above is neglected because the incidence is taken to be normal to the top surface, meaning no direct portion of the collimated incidence is absorbed by the radial wall.

After obtaining the intensity field through solution of the ERT, the incident radiation G at any location in the medium can be determined as follows, incorporating both diffuse and collimated contributions [12,13]:

$$G = \sum_{l=1}^M w^l I^l + I^C \exp(-\tau_z). \quad (7)$$

Similarly, radial heat flux Q_r and axial heat flux Q_z can be calculated in the following manner:

$$Q_r = \sum_{l=1}^M \mu^l w^l I^l, \quad Q_z = \sum_{l=1}^M \xi^l w^l I^l + I^C \exp(-\tau_z), \quad (8)$$

where the radial component is not directly impacted by the normally collimated incidence.

3. Phase-Function Normalization

The Mie phase function is generally a highly oscillatory function, which makes exact implementation difficult in any numerical scheme [22]. In order to facilitate numerical implementation, it is common to approximate the Mie phase function using a finite series of Legendre polynomials [22,24]. After DOM discretization, the diffuse scattering phase function $\Phi^{l'}$ can be calculated using the Legendre polynomial approximation as follows for the axisymmetric cylindrical medium [19,20]:

$$\Phi^{l'} = \frac{1}{2} \left[\sum_{i=0}^N C_i P_i(\cos \Theta_1^{l'}) + \sum_{i=0}^N C_i P_i(\cos \Theta_2^{l'}) \right], \quad (9)$$

where the coefficients C_i are determined from Mie theory, and the scattering angles $\Theta_1^{l'}$ and $\Theta_2^{l'}$ can be calculated from the direction cosines,

$$\begin{cases} \cos(\Theta_1^{l'}) = \mu^l \mu^{l'} + \eta^l \eta^{l'} + \xi^l \xi^{l'} \\ \cos(\Theta_2^{l'}) = \mu^l \mu^{l'} - \eta^l \eta^{l'} + \xi^l \xi^{l'} \end{cases} \quad (10)$$

The necessity of averaging the phase function between the two scattering angles comes from the axisymmetric nature of the problem. The discrete ordinate η^l is calculated via the relation $\eta^l = \pm[1 - (\mu^l)^2 - (\xi^l)^2]^{1/2}$, leading to two possible signs for the product $\eta^l \eta^{l'}$.

The collimated scattering phase function $\Phi^{l'c}$ can also be expressed using Legendre polynomials. For collimated incidence normal to the top surface, the collimated direction cosines are $\mu^C = 0$, $\eta^C = 0$, $\xi^C = -1$. Using Eqs. (9) and (10), along with these direction cosines, the expression for $\Phi^{l'c}$ becomes

$$\Phi^{l'c} = - \sum_{i=0}^N C_i P_i \xi^{l'}. \quad (11)$$

In order to ensure that scattered energy is conserved in the system after directional discretization, the diffuse scattering phase function $\Phi^{l'}$ must satisfy the following conservation relation for each discrete direction l' [22]:

$$\frac{1}{4\pi} \sum_{l=1}^M \Phi^{l'l} w^l = 1. \quad (12)$$

In addition to the conservation of scattered energy, the overall asymmetry factor of the phase function should not be altered after directional discretization. In order to preserve the asymmetry factor g of the original scattering phase function, the following relation must be satisfied for all discrete directions l' :

$$\frac{1}{4\pi} \sum_{l=1}^M \Phi^{l'l} \cos(\Theta^{l'l}) w^l = g, \quad (13)$$

where the quantity $\Phi^{l'l} \cos(\Theta^{l'l})$ is represented as follows, using the Legendre approximation and considering the two possible scattering angles as described in regards to Eqs. (9) and (10):

$$\Phi^{l'l} \cos(\Theta^{l'l}) = \frac{1}{2} \left[\sum_{i=0}^N C_i P_i(\cos \Theta_1^{l'l}) \cos(\Theta_1^{l'l}) + \sum_{i=0}^N C_i P_i(\cos \Theta_2^{l'l}) \cos(\Theta_2^{l'l}) \right]. \quad (14)$$

As scattering becomes highly anisotropic, the constraints given by Eqs. (12) and (13) are not always satisfied after DOM discretization. In order to ensure the conservation of scattered energy and asymmetry factor, phase-function normalization is introduced. Previously published techniques by Kim and Lee [16] and Wiscombe [17] were fashioned to explicitly satisfy the scattered energy—conservation relation of Eq. (12). However, detailed analyses by Boulet *et al.* [18] and Hunter and Guo [19,20] showed that these techniques distort the overall asymmetry factor and shape of the phase function, leading to inaccurate heat flux and intensity values.

Recently, Hunter and Guo [19,20] introduced a new normalization procedure that guarantees that the conservation relations of Eqs. (12) and (13) are conserved after DOM discretization. The diffuse scattering phase function is normalized as follows:

$$\bar{\Phi}^{l'l} = (1 + A^{l'l}) \Phi^{l'l}, \quad (15)$$

where the normalization parameters $A^{l'l}$ are such that $\bar{\Phi}^{l'l}$ satisfies the relations given in Eqs. (12) and (13). $\bar{\Phi}^{l'l}$ also satisfies a symmetry relation, namely $\bar{\Phi}^{l'l} = \bar{\Phi}^{ll}$. The normalization parameters that will accurately conserve both scattered energy and asymmetry factor can be determined using QR decomposition or via a pseudo-inverse technique, as described in the authors' previous works [19,20].

The previous works by the authors applied the normalization technique to cases involving diffuse irradiation in a steady state using both the DOM and FVM for ERT discretization, and mandated the necessity for conserving both scattered energy and the

asymmetry factor for highly anisotropic scattering media. For cases involving collimated incidence, special attention must be given to the normalization of $\Phi^{l'c}$, which must also satisfy the scattered-energy and asymmetry-factor relations of Eqs. (12)–(13) in which direction l' is replaced by l^c . Similarly, the collimated scattering phase function can be normalized as

$$\bar{\Phi}^{l'c} = (1 + A_C^{l'c}) \Phi^{l'c}. \quad (16)$$

The normalization parameters $A_C^{l'c}$ are independent of the previously described normalization parameters $A^{l'l}$ except in the case where the direction of collimated incidence coincides with one of the DOM discrete directions. In that case, it is not necessary to reevaluate the normalization parameters $A_C^{l'c}$.

4. Results and Discussion

The workstation used to determine all results in this study is a Dell Optiplex 780, with an Intel Core 2 processor and 4.0 gigabytes of RAM. The time-dependent ERT is solved using the TDOM with the S_{16} quadrature (288 total directions). For brevity, further details on discretization and solution using the TDOM are not presented here but can be found in great detail in [4,12,13,19]. The DOM scheme was implemented using the FORTRAN computing language, and the phase-function normalization parameters were determined using MATLAB's built-in function for pseudo-inversion. The parameters only have to be determined once for a given phase function, as they are solely dependent on the DOM quadrature scheme and phase-function asymmetry factor (medium properties such as scattering albedo and optical thickness can be freely changed without altering the normalization parameters). Once determined, the parameters are imported into FORTRAN for use in the DOM procedure. For the DOM S_{16} quadrature, the average computational time to determine and export the normalization parameters is 17.6 s for the diffuse normalization parameters of Eq. (15) and 0.62 s for the collimated normalization parameters of Eq. (16).

Figure 1 examines the conservation of both scattered energy and asymmetry factor through comparisons among three different normalization cases applied to the collimated phase function: no normalization, normalization with the old technique [16], and new normalization with the current technique. The conservation ratios are determined by averaging the values of the summations in Eqs. (12) and (13) for each direction l' over the theoretical or prescribed values, with a ratio of unity indicating that the quantity is exactly conserved. The four phase functions investigated in this study can be seen in Fig. 2 and have overall asymmetry factors of $g = 0.669723$, 0.7693 , 0.84534 , and 0.927323 , respectively. The Mie coefficients C_i for $g = 0.669723$ and $g = 0.84534$ are presented by Kim and Lee [25], while coefficients for

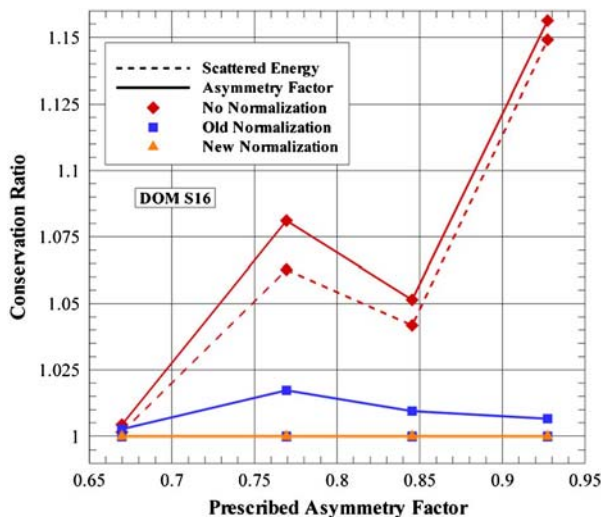


Fig. 1. (Color online) Conservation of scattered energy and asymmetry factor after collimated phase-function normalization.

$g = 0.7693$ and $g = 0.927323$ are presented by Lee and Buckius [26].

When normalization is neglected, both scattered energy and asymmetry factor are not accurately conserved for any of the four examined Legendre phase functions. For $g = 0.927323$, the conservation ratio for scattered energy differs from unity by 14.9%, while the conservation ratio for the asymmetry factor differs by 15.3%. These large skews for highly anisotropic scattering media indicate that the use of a normalization technique is imperative. When the old technique of Kim and Lee is applied, we see that scattered energy is explicitly conserved. This conforms to expectations, as this normalization technique was crafted specifically for this purpose. However, deviations from unity occur for the conservation of asymmetry factor. Although the conservation of asymmetry factor is improved over the case where

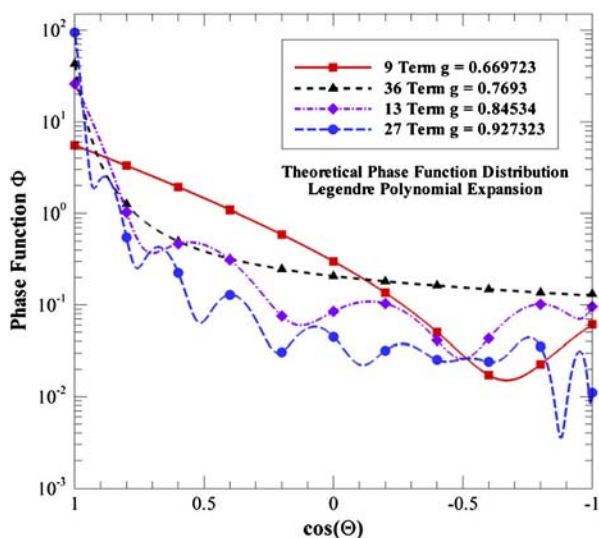


Fig. 2. (Color online) Legendre polynomial phase-function distributions.

normalization is neglected, results by Boulet *et al.* [18] and Hunter and Guo [19] showed that even minor deviations in asymmetry factor after discretization can lead to vastly inaccurate results for strong scattering media according to the isotropic scattering rule [27]. When the new technique of Hunter and Guo is applied, both scattered energy and the asymmetry factor are accurately conserved.

For validation purposes, the algorithm was applied to a test case presented in Jendoubi *et al.* [28]. For this case, a cylindrical enclosure with aspect ratio $R/H = 0.5$ subject to a normal collimated incidence on the top surface ($z = 0$) was analyzed. The optical depth $\tau = \beta R$ and scattering albedo ω of the enclosed gray medium were taken to be unity. The radial and bottom walls of the enclosure are cold, diffuse, and nonreflecting. The spatial grid used for this analysis was $(N_r \times N_z) = (40 \times 80)$. The steady-state results were determined by neglecting the temporal term in the ERT and using an iterative solution procedure. No phase-function normalization was implemented for this case. For all following results, radial location r and axial location z are nondimensionalized as follows: $r^* = r/R$, $z^* = z/H$.

Figure 3 compares nondimensional radial wall heat flux $\bar{Q}_r(r^* = 1)$ versus axial location z^* for various phase functions. The heat flux at the radial wall has been nondimensionalized by the collimated intensity I^C . Results were also calculated using the FVM with 288 directions in order to further validate our code. For all phase functions and axial locations, it is observed that our numerical predictions conform accurately to the predictions presented in the literature. In addition, the results calculated with the DOM correspond accurately to those determined using the FVM, with a maximum percentage difference of 1.75% occurring for $g = 0.669723$. The accuracy of the DOM solutions when compared to both

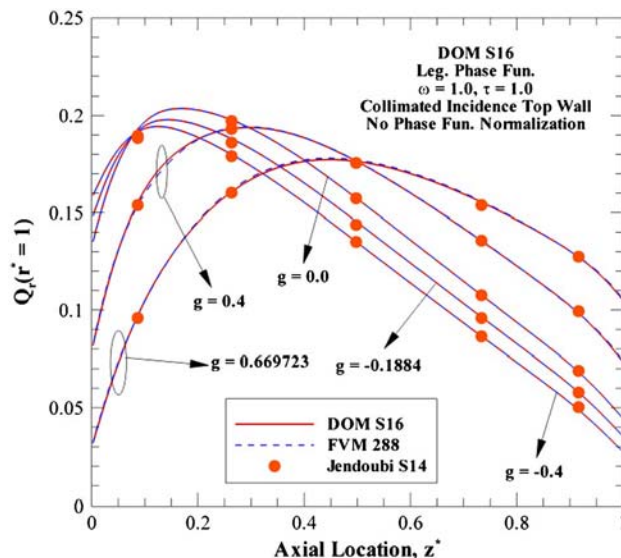


Fig. 3. (Color online) Comparison of radial wall heat flux versus axial location determined from numerical predictions and literature [28].

the previously published results in Jendoubi *et al.* [28] and the calculated FVM results indicate that our DOM code is treating the collimated component properly and give the authors confidence in the forthcoming results.

Attention is now turned to the biological tissue cylinder subject to a collimated incidence at the top surface, with dimensions $R = 5$ mm and $H = 2$ mm. The optical properties were assumed to be those of human dermis [24]: $\beta = 18.97$ mm⁻¹, $\omega = 0.9858$. The total optical depth $\tau = \beta H$ of the medium is then calculated as $\tau = 37.94$. The spatial grid used for all simulations is $(N_r \times N_z) = (150 \times 60)$ in order to both fully capture accurate results and keep the step size equal in both the radial and axial directions. For all transient results, a nondimensional time step of $\Delta t^* = c\Delta t/H = 0.00893$ was chosen in order to satisfy the following criterion to ensure the traveling distance of light between two successive time steps is not greater than the control-volume size [12]:

$$\Delta t^* \leq \min(\Delta r^*, \Delta z^*), \quad (17)$$

where $\Delta r^* = \Delta r/R$ and $\Delta z^* = \Delta z/H$. The refractive index of tissue is taken to be 1.4, and thus the speed of light through the medium can be calculated as 0.214 m/ns.

Figure 4 depicts steady-state, nondimensional radial wall heat flux versus axial location for the four previously mentioned Legendre phase functions. Three overall normalization cases are considered for comparison: no normalization, diffuse scattering phase-function normalization only, and full normalization of both the diffuse and collimated scattering phase functions. The effect of the collimated incidence can be seen close to the top wall ($z = 0$) for all the four asymmetry factors. As the asymmetry factor increases, radiant energy is more strongly scattered

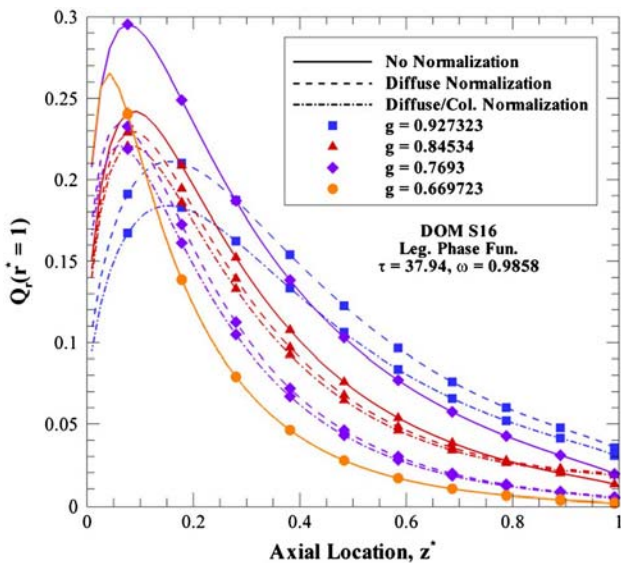


Fig. 4. (Color online) Steady-state radial wall heat flux versus axial location for various asymmetry factors and various normalization cases.

away from the top wall and through the tissue medium, leading to decreases in heat flux near the top wall of the cylinder and increases near the bottom wall. The axial location of the maximum heat flux increases as the asymmetry factor increases, again due to the increase in the strength of forward scattering. For example, the maximum heat flux occurs at $z/H = 0.075$ for $g = 0.669723$ and at $z/H = 0.15$ for $g = 0.927323$. The large optical thickness of tissue hinders the propagation of radiant energy through the medium, leading to smoothly decreasing heat flux profiles over the depth of the medium.

The effects of both diffuse and collimated phase-function normalization can also be seen in Figure 4. For $g = 0.669723$, heat flux profiles predicted using no normalization, diffuse normalization only, and full normalization are nearly identical, with a maximum percent difference of 0.50% occurring at the bottom wall for the case where normalization is entirely neglected. This matches results presented for diffuse irradiation by Hunter and Guo [19], who found that normalization for the DOM was not necessary for asymmetry factors less than 0.7 when a Henyey–Greenstein phase function was adopted. As the asymmetry factor increases, however, discrepancies between the predicted heat flux profiles start to appear. Using the fully normalized case as a basis, maximum differences of 0.28%, 7.30%, 4.28%, and 15.5% are witnessed when the diffuse phase function is solely normalized for $g = 0.669723$, 0.7693, 0.84534, and 0.927323, respectively. When no normalization is implemented, the overall differences increase dramatically to 0.50%, 316.70%, 29.92%, and 1770.98%, respectively. In fact, the discrepancy caused by a lack of conservation of diffuse scattered energy for $g = 0.927323$ is so great that the curve does not appear on the plot. These large differences mandate the necessity of conserving scattered energy and asymmetry factor for the diffuse phase function. The still significant differences inherent when the collimated phase function is not normalized indicate that sole normalization of the diffuse phase function is insufficient. Normalization of the collimated phase function should be introduced to exactly conserve scattered energy and asymmetry factor in the entire system.

Figure 5 depicts transient radial-wall heat flux profiles versus axial location for $g = 0.927323$ at various nondimensional times. Profiles are presented for the case where both the diffuse and collimated phase function are normalized, and for diffuse normalization only. Because the case where normalization was neglected produced extremely distorted and inaccurate results, all further results will be presented without that case to showcase the importance of conserving the asymmetry factor and scattered energy for the collimated scattering phase function. As the time increases, an increase in both the heat flux magnitude and the propagation depth of radiant energy away from the top wall is witnessed. At small time ($\Delta t^* = 0.3125$), the heat flux near the bottom wall

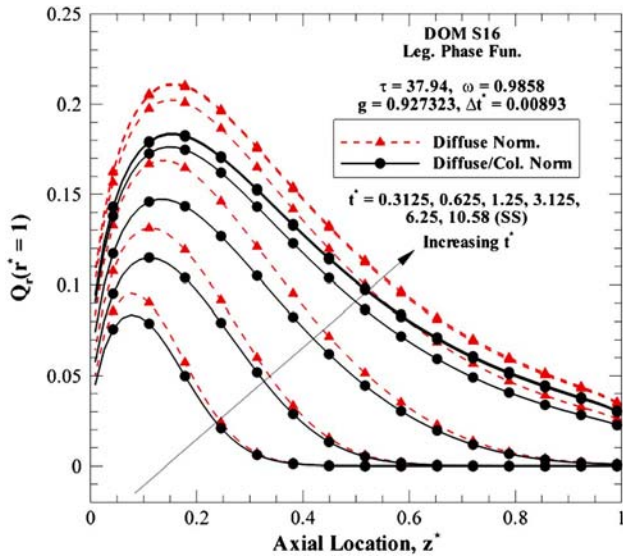


Fig. 5. (Color online) Transient radial wall heat flux versus axial location for $g = 0.927323$ with and without collimated phase-function normalization.

is negligible due to the lack of propagation of radiant energy to this wall. When the steady-state solution seen in Fig. 5 is reached at $\Delta t^* = 10.58$, energy has propagated through the tissue medium, leading to appreciable values of heat flux throughout.

Figure 6 depicts nondimensional heat flux at the bottom wall $-Q_z(z^* = 1)$ versus radial location for various times with $g = 0.927323$. The negative sign indicates that the net direction of flux is into the wall. Heat flux profiles are the largest near the centerline of the tissue cylinder and smallest near the radial wall due to the cold, diffusely reflecting boundary condition. At small times, the heat flux at the bottom wall is miniscule due to the fact that the medium is optically thick and propagation of radiant energy has not yet reached the boundary. The effect of the reflecting radial wall becomes more pronounced for larger times due to an increase of energy scattering towards the radial wall.

As seen from Figs. 5 and 6, profiles generated without collimated phase-function normalization overpredict profiles generated with full normalization for all times.

For applications such as the laser ablation of cancerous cells, it is important to control the amount of radiant energy absorbed by surrounding tissue so that healthy tissue is not damaged. The radiant energy absorption rate can be determined as follows:

$$g_{\text{rad}} = \beta(1 - \omega)(G - 4\pi I_b), \quad (18)$$

where g_{rad} is the volumetric radiation energy absorption rate and G is the incident radiation. For this analysis, the medium is taken as cold ($I_b = 0$) so that the sole effects of radiative transfer can be examined. Further, g_{rad} can be nondimensionalized by the collimated intensity I^C and medium depth H as follows:

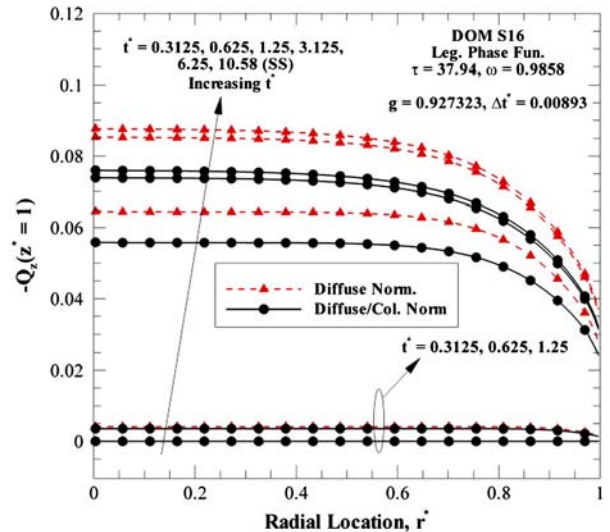


Fig. 6. (Color online) Transient bottom wall heat flux versus radial location for $g = 0.927323$ with and without collimated phase-function normalization.

$$g_{\text{rad}}^* = \frac{\beta(1 - \omega)G}{4\pi I^C / H}. \quad (19)$$

Figure 7 plots the radiation energy absorption rate profiles in steady state versus radial location for three different axial locations ($z^* = 0, 0.5, 1$) evaluated for various asymmetry factors. Both the diffuse and collimated phase functions were normalized for this analysis using Hunter and Guo's technique. At the top wall ($z^* = 0$), an increase in asymmetry factor corresponds directly to a decrease in energy absorption due to the fact that radiation scatters more strongly away from the wall at high asymmetry factors. At the axial midplane ($z^* = 0.5$) and bottom wall ($z^* = 1$), the opposite trend is witnessed, as expected. The effect of the reflecting radial wall is manifested as a decrease in energy absorption at the tissue radius. The energy absorption rate has higher magnitude at the top wall due to the presence of the collimated source, and lowest magnitude at the bottom wall due to the large propagation distance through the optically thick medium.

Figure 8 depicts the time-dependent energy absorption rate profiles at the radial centerline for three axial locations and various asymmetry factors. For all axial locations and asymmetry factors, the absorbed energy rate at the centerline increases with increasing time. At small times, the energy absorption rate at both the axial midplane and bottom wall are miniscule, while the rate at the top wall is larger due to the proximity to the collimated incidence. At the top wall, an increase in the asymmetry factor produces a decrease in the magnitude of energy absorption, whereas the opposite trend is seen at the other axial locations. The profiles generated with no collimated phase-function normalization again overpredict the profiles generated with the full normalization technique for all asymmetry factors shown and all axial locations.

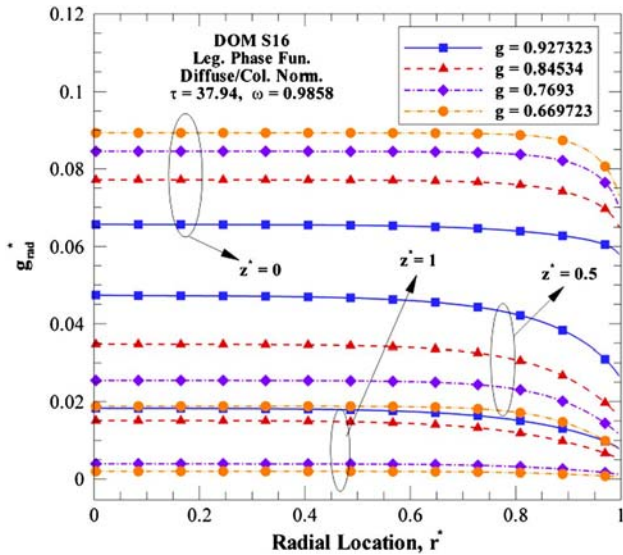


Fig. 7. (Color online) Energy absorption rate versus radial location for various asymmetry factors.

An interesting trend is seen when comparing percent differences between profiles generated with and without collimated phase-function normalization at the different axial locations. For $g = 0.927323$, the profile generated with only diffuse normalization overpredicts the fully normalized case by 16.65%, 15.56%, and 15.43% for $t^* = 0.3125, 3.125,$ and 12.5 , respectively, at the bottom wall. A similar strict decrease in percent difference with time is seen for the axial midplane, with the percent differences of 16.43%, 15.45%, and 15.41% at the same times having slightly smaller magnitudes. At the top wall, however, the opposite trend is seen. For the same nondimensional times, the percent differences are 6.28%, 8.11%, and 8.47%, respectively. The percent difference strictly increases with time at the top wall,

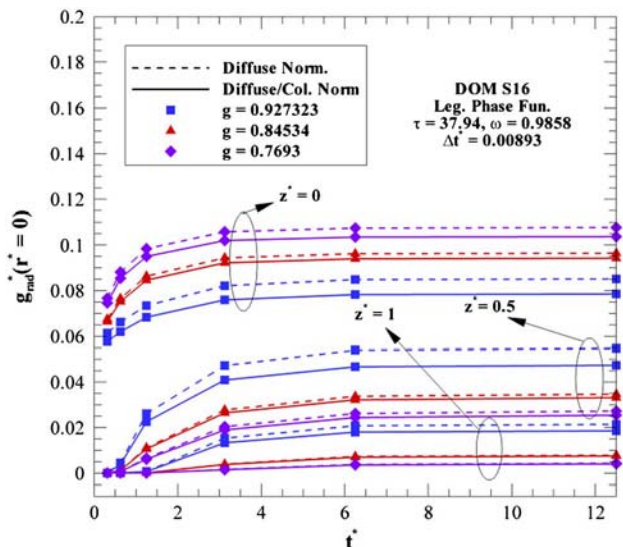


Fig. 8. (Color online) Energy absorption rate at the radial centerline for various times and asymmetry factors with and without collimated phase-function normalization.

conversely to the previous axial locations. In addition, the difference between the normalization cases is less pronounced at the top wall for all times. Similar trends are seen for $g = 0.7693$ and $g = 0.84534$.

Recently, Rath and Mahapatra [21] developed a new formulation of the divergence of radiative heat flux for ultrafast radiative transfer. To determine their expression, Eq. (1) is first integrated over all solid angles. Performing said integration and rearranging terms, the following expression is obtained:

$$\begin{aligned} \frac{1}{c} \frac{\delta}{\delta t} \int_{4\pi} I(\mathbf{r}, \hat{\mathbf{s}}, t) d\Omega + \nabla \cdot \int_{4\pi} I(\mathbf{r}, \hat{\mathbf{s}}, t) \hat{\mathbf{s}} d\Omega \\ = -\beta \int_{4\pi} I(\mathbf{r}, \hat{\mathbf{s}}, t) d\Omega + \sigma_a \int_{4\pi} I_b(\mathbf{r}, t) d\Omega \\ + \frac{\sigma_s}{4\pi} \int_{4\pi} I(\mathbf{r}, \hat{\mathbf{s}}', t) \left(\int_{4\pi} \Phi(\hat{\mathbf{s}}', \hat{\mathbf{s}}) d\Omega \right) d\Omega'. \end{aligned} \quad (20)$$

Noting that $\int_{4\pi} I(\mathbf{r}, \hat{\mathbf{s}}, t) \hat{\mathbf{s}} d\Omega = q_{\text{rad}}$, $\int_{4\pi} I_b(\mathbf{r}, t) d\Omega = 4\pi I_b(\mathbf{r}, t)$, and $\int_{4\pi} \Phi(\hat{\mathbf{s}}, \hat{\mathbf{s}}') d\Omega = 4\pi$ from the conservation of scattered energy, Eq. (20) reduces to the following form [using $\sigma_s = \beta\omega$ and $\sigma_a = \beta(1-\omega)$]:

$$\begin{aligned} \frac{1}{c} \frac{\delta}{\delta t} \int_{4\pi} I(\mathbf{r}, \hat{\mathbf{s}}, t) d\Omega + \nabla \cdot q_{\text{rad}} \\ = -\beta \int_{4\pi} I(\mathbf{r}, \hat{\mathbf{s}}, t) d\Omega + 4\pi\beta(1-\omega)I_b(\mathbf{r}, t) \\ + \beta\omega \int_{4\pi} I(\mathbf{r}, \hat{\mathbf{s}}', t) d\Omega'. \end{aligned} \quad (21)$$

Rearranging Eq. (21) and using the definition for incident radiation $G(\mathbf{r}, t) = \int_{4\pi} I(\mathbf{r}, \hat{\mathbf{s}}, t) d\Omega$, the final expression for the divergence of radiative heat flux becomes

$$\nabla \cdot q_{\text{rad}} = \beta(1-\omega)(4\pi I_b - G) - \frac{1}{c} \frac{\delta G}{\delta t}. \quad (22)$$

The first term on the right-hand side is the traditional formulation of divergence of radiative heat flux for steady-state ERT [the same as what we have called g_{rad} in Eq. (18), only with the opposite sign]. The second transient term on the right-hand side is a new addition. Rath and Mahapatra thought that this transient term directly contributes to the energy deposition in the medium, impacting the calculation of temperature in the medium from the energy equation. In the authors' opinion, however, this term is not related to local energy deposition; instead, we believe this term describes the propagation of radiant energy with a wave through the medium. The authors' belief is that the transient term above accounts for the amount of propagating energy that is "trapped" in a given control volume at a specific time instant, which will travel to adjacent control volumes at subsequent time instants and not be physically absorbed by the medium at that location. This notion is supported by the fact that while there

should be no energy deposition in the medium for a purely scattering situation ($\omega = 1$), the addition of the transient term gives a nonzero value to the divergence of radiative heat flux for time instants prior to the steady-state condition. In addition, it should be noted (as pointed out by an anonymous reviewer of this paper) that this term is analogous to Maxwell's "capacitive term" that represents stored wave energy that will not necessarily be ultimately dissipated in the medium.

Figure 9 plots the divergence of radiative heat flux at the radial centerline for various nondimensional times with $g = 0.927323$. Profiles are generated with and without the propagation term listed in Eq. (22) and with both the diffuse and collimated scattering phase functions normalized. When the propagation term is neglected (as to produce profiles using the prior definition of energy absorption), we see a general increase in energy deposition with increasing time. At small time, energy deposition is higher near the top wall due to the collimated source but negligible at greater depths into the tissue sample. As time increases and radiant energy propagates further through the medium, the divergence of radiative heat flux increases at all axial locations until a steady state is reached. This conforms to expectations, as the overall amount of energy absorbed by the cold medium should strictly increase with increasing time.

When the propagation term is included, a much different phenomenon is noticed. At small times, near the collimated source, there is a large spike in energy deposition due to the high magnitude of the propagation term (the product $1/c\Delta t$ is extremely large for small time steps, greatly magnifying small changes in incident radiation G between subsequent time instants). As time increases and the problem approaches a steady-state, the contribution of the propagation term rapidly decreases, leading to decreasing divergence of radiative heat flux near the collimated source. In fact, when analyzing divergence profiles for small times, a wave-like propagation of radiant energy can be witnessed, with the high spike at small time due to the high magnitude of radiant energy propagating away from the collimated source. As time increases, the radiant energy is scattered in all directions, leading to a decrease in overall magnitude of the spike produced by the propagation term.

The pattern of decreasing energy deposition with increasing time counters the general idea of energy deposition for the cold medium. Energy is constantly absorbed by the medium during the temporal process, which should lead to consistently increasing values of divergence. For this reason, and on account of the example for pure scattering mentioned above, the authors believe that the transient term in Eq. (22) is merely a description of the propagation of the energy wave through the medium or of the propagating energy that is "trapped" in a certain control volume at a certain time instant but that will leave the control

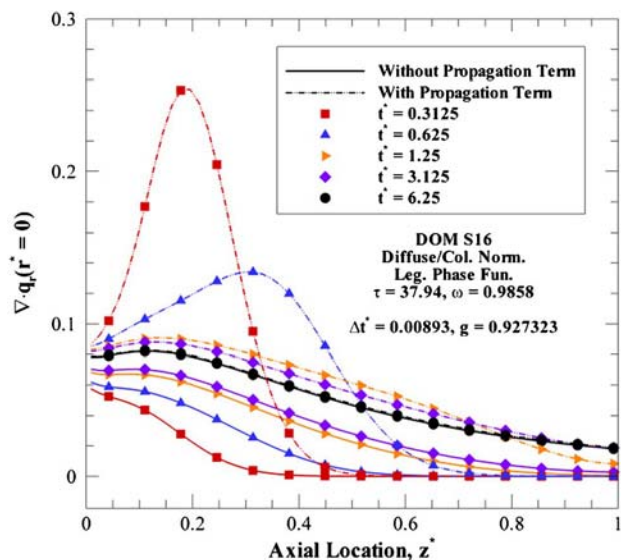


Fig. 9. (Color online) Effect of propagation term on radial centerline divergence of radiative heat flux.

volume subsequently. The authors believe that the overall formulation of divergence of radiative heat flux given in Eq. (22) is correct but that the propagation term will not contribute to local temperature change due to the fact that it is not a direct energy deposition in the medium. For steady-state radiative transfer, Eq. (22) will go back to the conventional expression of energy absorption [Eq. (18)]. In ultrafast radiative transfer, however, the divergence of radiative heat flux is not equivalent to local energy deposition. This formulation by Rath and Mahapatra brings forth the notion that the divergence of heat flux contains two components: local energy deposition and wave-like energy propagation.

5. Conclusions

In this study, phase-function normalization was applied to the TDOM for ultrafast collimated radiative transfer analysis. The phase-function normalization technique introduced by Hunter and Guo for the diffuse scattering phase function was further applied to the collimated phase function to gauge the importance of normalization when a collimated source is applied to a turbid medium. Sole normalization of the diffuse scattering phase function does not impact the collimated phase function, mandating further normalization to ensure that the collimated phase function satisfies conservation of scattered energy and asymmetry factor.

Both heat flux and energy deposition profiles, determined for various asymmetry factors, were compared to investigate the importance of collimated phase-function normalization. As the asymmetry factor increased, lack of diffuse and collimated phase-function normalization produced discrepancies in steady-state heat flux profiles, with differences over 100% when normalization was altogether neglected and 16% when only the diffuse normalization was considered for $g = 0.927323$. When transient profiles

were investigated, the percent difference between diffuse only and full normalization cases exceeded 10% for all radial and axial locations and times for $g = 0.927323$. It was found that the axial location had a strong impact on the difference between energy deposition calculated with and without collimated phase-function normalization. Near the collimated source, the percentage difference for all asymmetry factors decreased with increasing time, while at locations far from the source the opposite trend was witnessed. All of the results dictate that it is imperative to use phase-function normalization techniques that will accurately conserve both scattered energy and asymmetry factor for both the collimated and diffuse radiation components.

The expression of the divergence of radiative heat flux is examined. While the addition of a transient term to the divergence of radiative heat flux is plausible, this term is not related to local energy deposition. Rather, it simply describes the propagation of radiant energy by a wave through the medium. When wave propagation is negligible, the transient term drops and the divergence of radiative heat flux goes back to the negative of local energy deposition in a steady state. It is important to note that the propagation term should not be used as part of the radiative source affecting medium temperature even in ultrafast radiative heat transfer calculations.

References

1. S. L. Jacques, "Time resolved propagation of ultrashort laser pulses within turbid tissues," *Appl. Opt.* **28**, 2223–2229 (1989).
2. Y. Yamada, "Light-tissue interaction and optical imaging in biomedicine," *Annu. Rev. Heat Transfer* **6**, 1–59 (1995).
3. K. Mitra and S. Kumar, "Development and comparison of models for light-pulse transport through scattering-absorbing media," *Appl. Opt.* **38**, 188–196 (1999).
4. K. H. Kim and Z. Guo, "Ultrafast radiation heat transfer in laser tissue welding and soldering," *Num. Heat Transfer A* **46**, 23–40 (2004).
5. H. Quan and Z. Guo, "Fast 3-D optical imaging with transient fluorescence signals," *Opt. Express* **12**, 449–457 (2004).
6. K. H. Kim and Z. Guo, "Multi-time-scale heat transfer modeling of turbid tissues exposed to short-pulsed irradiations," *Comput. Meth. Prog. Bio.* **86**, 112–123 (2007).
7. M. Jaunich, S. Raje, K. H. Kim, K. Mitra, and Z. Guo, "Bio-heat transfer analysis during short pulse laser irradiation of tissues," *Int. J. Heat Mass Transfer* **51**, 5511–5521 (2008).
8. J. C. Chai, H. S. Lee, and S. V. Patankar, "Finite volume method for radiation heat transfer," *J. Thermophys. Heat Transfer* **8**, 419–425 (1994).
9. Z. Guo and S. Kumar, "Radiation element method for transient hyperbolic radiative transfer in plane parallel inhomogeneous media," *Numer. Heat Transfer B* **39**, 371–387 (2001).
10. P-F. Hsu, Z. Tan, and J. P. Howell, "Radiative transfer by the YIX method in non-homogeneous, scattering and non-gray medium," *J. Thermophys. Heat Transfer* **7**, 487–495 (1993).
11. B. G. Carlson and K. D. Lathrop, "Transport theory—the method of discrete-ordinates," in *Computing Methods in Reactor Physics*, H. Greenspan, C. N. Kelber, and D. Okrent, eds. (Gorden and Breach, 1968).
12. Z. Guo and S. Kumar, "Discrete-ordinates solution of short-pulsed laser transport in two-dimensional turbid media," *Appl. Opt.* **40**, 3156–3163 (2001).
13. Z. Guo and S. Kumar, "Three-dimensional discrete ordinates method in transient radiative transfer," *J. Thermophys. Heat Transfer* **16**, 289–296 (2002).
14. J. Jiao and Z. Guo, "Modeling of ultrashort pulsed laser ablation in water and biological tissues in cylindrical coordinates," *Appl. Phys. B* **103**, 195–205 (2011).
15. M. Akamatsu and Z. Guo, "Ultrafast radiative heat transfer in three-dimensional highly-scattering media subjected to pulse train irradiation," *Num. Heat Transfer A* **59**, 653–671 (2011).
16. T. K. Kim and H. Lee, "Effect of anisotropic scattering on radiative heat transfer in two-dimensional rectangular enclosures," *Int. J. Heat Mass Transfer* **31**, 1711–1721 (1988).
17. W. J. Wiscombe, "On initialization, error and flux conservation in the doubling method," *J. Quant. Spectrosc. Radiat. Transfer* **16**, 637–658 (1976).
18. P. Boulet, A. Collin, and J. L. Consalvi, "On the finite volume method and the discrete ordinates method regarding radiative heat transfer in acute forward anisotropic scattering media," *J. Quant. Spectrosc. Radiat. Transfer* **104**, 460–473 (2007).
19. B. Hunter and Z. Guo, "Conservation of asymmetry factor in phase function normalization for radiative transfer analysis in anisotropic scattering media," *Int. J. Heat Mass Transfer* **55**, 1544–1552 (2012).
20. B. Hunter and Z. Guo, "Reduction of angle splitting and computational time for the finite volume method in radiative transfer analysis via phase function normalization," *Int. J. Heat Mass Transfer* **55**, 2449–2460 (2012).
21. P. Rath and S. K. Mahapatra, School of Mechanical Sciences, Indian Institute of Technology, Bhubaneswar, Bhubaneswar, Odisha—751 013, India (personal communication, 2011).
22. M. F. Modest, *Radiative Heat Transfer* 2nd ed. (Academic, 2003).
23. B. Hunter and Z. Guo, "Comparison of discrete-ordinates method and finite volume method for steady-state and ultrafast radiative transfer analysis in cylindrical coordinates," *Num. Heat Transfer B* **59**, 339–359 (2011).
24. W. F. Cheong, S. A. Prahl, and A. J. Welch, "A review of the optical properties of biological tissues," *IEEE J. Quantum Electron* **26**, 2166–2185 (1990).
25. T. K. Kim and H. Lee, "Scaled isotropic results for two-dimensional anisotropic scattering media," *J. Heat Transfer* **112**, 721–727 (1990).
26. H. Lee and R. O. Buckius, "Scaling anisotropic scattering in radiation heat transfer for a planar medium," *J. Heat Transfer* **104**, 68–75 (1982).
27. Z. Guo and S. Kumar, "Equivalent isotropic scattering formulation for transient short-pulse radiative transfer in anisotropic scattering planar media," *Appl. Opt.* **39**, 4411–4417 (2000).
28. S. Jendoubi, H. S. Lee, and T. K. Kim, "Discrete ordinates solutions for radiatively participating media in a cylindrical enclosure," *J. Thermophys. Heat Transfer* **7**, 213–219 (1993).